SPATIAL INSTABILITY OF TWO-PHASE MIXING LAYERS

Thomas Otto*, Maurice Rossi°, Thomas Boeck*

*Dept. of Mechanical Engineering, TU Ilmenau, P.O. Box 100565, 98684 Ilmenau, Germany
email: thomas.otto@tu-ilmenau.de, thomas.boeck@tu-ilmenau.de

°Institut Jean Le Rond D'Alembert, Université Pierre et Marie Curie,
4 place Jussieu, 75252 Paris Cedex 05, France, email: maurice.rossi@upmc.fr

ABSTRACT
The instability of viscous two-phase mixing layers is studied in the planar case using two-dimensional spatial and temporal linear stability analysis. The basic flow is characterized by finite boundary layer sizes on either side of the interface, which are modelled by error function profiles. Surface tension effects are neglected. The spatial instability code is validated with results from one-phase shear layers. At matched densities it is found that the viscous instability mechanism associated with viscosity stratification can cause absolute instability without reversed flow. The effect of an additional basic velocity defect on the interface is examined for viscosity and density ratios close to air and water. Temporal instability results are hardly changed by this defect, but spatial growth rates can be significantly enhanced.

INTRODUCTION

The atomization of liquids by fast gas streams is a complex and technologically important two-phase flow, especially in the context of combustion in thermal engines. A better understanding of spray formation can have significant implications for the choice of process parameters and injector designs. Such flows have therefore received much attention, and considerable progress has been made in recent years [1, 2, 3]. This is in part due to the development of sophisticated experimental techniques for optical flow measurement and also due to the development of accurate numerical methods for the simulation of two-phase flows. Nonetheless, simulations of atomization are still not fully capable of resolving the multitude of length scales in such flows, or reaching the experimental high Reynolds numbers. Moreover analyzing direct numerical simulation results is a challenging task in itself.

Theoretical models for liquid atomization have to address increasingly complex deformations of the liquid-gas interface. The starting point is the destabilization of the planar (or cylindrical) interface near the nozzle, where liquid and gas come into contact. Experiments have shown that the initial stage is characterized by perturbations belonging to a particular range of wavelengths [2, 4]. Such perturbations set the lengthscale for subsequent events leading to the formation of liquid ligaments and droplets. Under the assumption of parallel flow, predictions for this range of wavelengths and the associated temporal/spatial growth rates are obtained by solving a standard linear hydrodynamic stability problem. This aspect has received considerable attention in the literature. Apart from its significance for theoretical models, the linear instability of such two-phase mixing layers also provides an important test case for the verification of numerical codes for direct simulation of two-phase flows [5, 6].

The linear instability of parallel two-phase mixing layers has been frequently treated as a two-dimensional temporal stability problem with real wavenumber, which considerably simplifies the formulation and analysis. Moreover, inviscid flow is frequently assumed because of the high Reynolds numbers in the applications [7]. Viscous effects have recently been studied in the temporal instability framework [8, 9]. It turned out that a certain viscous mechanism – identified previously by Hooper and Hinch for the unbounded plane Couette flow of two layered liquids – is also present in the viscous two-phase mixing layer. This so-called H-mode instability depends on the continuity of shear stresses and tangential velocities at the interface and leads to a vorticity perturbation when the interface is perturbed. Differential advection of this additional vorticity by the basic flow can amplify the interface perturbation [10, 11]. The H-mode appears in addition to inviscid or Tollmien-Schlichting modes, and can be detected using its specific dependence on the Reynolds number.

Other recent works have treated the inviscid instability in the spatial framework, i.e. with a complex wavenumber and real frequency of the imposed perturbation [12, 13]. This approach is clearly preferable since the underlying problem is a spatially developing flow. Indeed the structure of spatial modes should be more related to the experimental profiles than temporal stability modes. A two-dimensional spatial instability analysis is thus applied on a viscous two-phase mixing layer in the present paper. The instability mechanism due to viscosity stratification is thus taken into account in the spatial framework and the role of the H-mode as a source of absolute instability is illustrated. In addition, the effect of a velocity defect in the basic velocity profile is studied in the temporal as well as spatial stability frameworks.
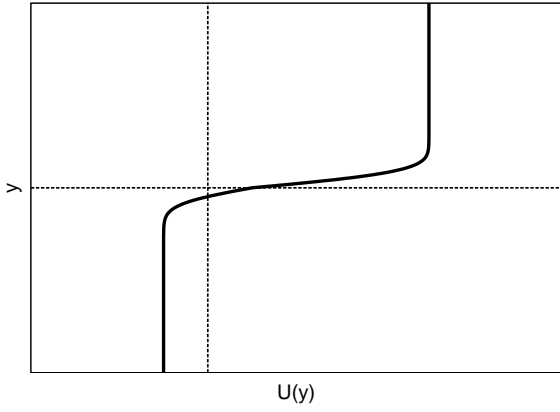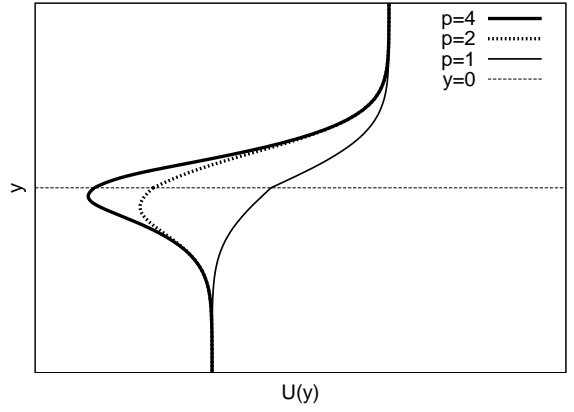
Figure 1: Error function basic velocity profile.

Figure 2: Generalized basic velocity profile.

BASIC VELOCITY PROFILES

In atomization experiments, the velocity distributions of gas and liquid at the nozzle exit or tip of the splitter plate are characterized by boundary layers in each fluid originating from the rigid wall separating the fluids upstream. Appropriate basic velocity profiles for the stability analysis of two-phase mixing layers are therefore characterized by finite boundary layer sizes.

In recent works on the temporal stability problem the planar basic velocity distribution was modelled by error functions in each fluid resulting in a profile similar to Figure 1 [8, 9]. The analytical expression for such a basic velocity profile is

$$U_1(y) = W^* + U_1^* \, \mathrm{erf}(y/\delta_1), \quad (y < 0) \tag{1}$$

$$U_2(y) = W^* + U_2^* \, \mathrm{erf}(y/\delta_2), \quad (y > 0) \tag{2}$$

where quantity W^* corresponds to the velocity at the liquid-gas interface. This position coincides with the streamwise coordinate axis $y = 0$. The subscripts 1 and 2 denote the lower liquid and the upper gas phase respectively. Quantities $U_1^\infty = W^* - U_1^*$ and $U_2^\infty = W^* + U_2^*$ are the far field velocities of the liquid and gas layer. Finally the velocity increments U_1^* and U_2^* in each layer are coupled to the boundary layer thicknesses δ_1 and δ_2 to comply with the shear stress continuity at the interface, i.e.

$$\frac{\mu_1 U_1^\star}{\delta_1} = \frac{\mu_2 U_2^\star}{\delta_2}. \tag{3}$$

When the non-dimensionalization procedure is based on the length and velocity scales of the top layer

$$\{x, y\} = \delta_2\{\hat{x}, \hat{y}\}, \qquad \{U_j, u'_j, v'_j\} = U_2^*\{\hat{U}_j, \hat{u}'_j, \hat{v}'_j\},$$

$$t = \frac{\delta_2}{U_2^*}\hat{t}, \quad \text{and} \quad p'_j = \rho_2 U_2^{*2}\hat{p}'_j, \quad j = 1, 2,$$

the error function profile reads in nondimensionalized form as

$$U_1(y) = \frac{W}{V} + \frac{1}{V} \, \mathrm{erf}(ny), \quad -L_1 \leq y \leq 0, \tag{4}$$

$$U_2(y) = \frac{W}{V} + \mathrm{erf}(y), \quad 0 \leq y \leq L_2, \tag{5}$$

where the quantities

$$r = \frac{\rho_2}{\rho_1}, \quad m = \frac{\mu_2}{\mu_1} \quad \text{and} \quad n = \frac{\delta_2}{\delta_1} \tag{6}$$

correspond to ratios of densities, dynamic viscosities and boundary layer sizes and $V \equiv U_2^*/U_1^*$, $W \equiv W^*/U_1^*$. In addition the shear balance (3) reads in nondimensional form as

$$V = \frac{n}{m} \tag{7}$$

Note that the fluid domain is assumed to be large compared with the boundary layer size i.e. $\frac{1}{n} << L_1$ and $1 << L_2$.

As discussed in Ref. [9], the choice of the above profile is appropriate only after some distance from the splitter plate. Right at the tip of the splitter plate the velocity distribution is similar to a wake profile because of the no-slip condition on this plate. To take this velocity defect into account, a generalized velocity distribution is proposed on the basis of the previous error-function modelling, which is shown in Figure 2. To mimick the finite thickness of the splitter plate, and also to maintain the shear balance, a vorticity layer is introduced near both side of the interface of thicknesses δ_1' in the lower fluid, i.e. fluid 1 and δ_2' in the top fluid, i.e. fluid 2. The expressions for the generalized basic velocity profile reads as follows

$$U_1(y) = W^* - U_1^* \, \mathrm{erf}\left(\frac{y}{\delta_1}\right) + U_d^*\left[1 + \mathrm{erf}\left(\frac{y}{\delta_1'}\right)\right], \tag{8}$$

$$U_2(y) = W^* + U_2^* \, \mathrm{erf}\left(\frac{y}{\delta_2}\right) + U_d^*\left[1 - \mathrm{erf}\left(\frac{y}{\delta_2'}\right)\right]. \tag{9}$$

The size of the prefactor U_d^* is determined by the shear balance at the interface

$$U_d^* = \frac{\frac{\mu_2 U_2^*}{\delta_2} + \frac{\mu_1 U_1^*}{\delta_1}}{\frac{\mu_2}{\delta_2'} + \frac{\mu_1}{\delta_1'}}. \tag{10}$$

Indeed, for the generalized basic flow, the shear balance is maintained by the choice of U_d^* and not by the choice of V as previously. Note that quantities $U_1^\infty = W^* + U_1^*$ and $U_2^\infty = W^* + U_2^*$ now stand for the far field velocities of the liquid and gas layer respectively. Finally, the defect thicknesses δ_1' and δ_2' are assumed smaller than the boundary layer thicknesses δ_1 and δ_2. The ratio

$$p = \frac{\delta_j}{\delta_j'} \geq 1 \tag{11}$$

of the boundary layer thickness to the vorticity sheet thickness is assumed identical in both fluids.

In nondimensional form, the generalized velocity profile reads

$$U_1(y) = \frac{W}{V} - \frac{1}{V}\operatorname{erf}(ny) + \left(\frac{m/n + 1/V}{p}\right)\frac{1 + \operatorname{erf}(npy)}{m/n + 1},$$ (12)

$$U_2(y) = \frac{W}{V} + \operatorname{erf}(y) + \left(\frac{m/n + 1/V}{p}\right)\frac{1 - \operatorname{erf}(py)}{m/n + 1},$$ (13)

where $V \equiv U_2^*/U_1^*$, $W \equiv W^*/U_1^*$.

STABILITY EIGENVALUE PROBLEM

The linear stability problem is formulated in two dimensions, i.e. we assume perturbations about the basic flow in the form of streamfunctions ψ_1 and ψ_2. The streamwise and cross-stream velocity components u and v are defined by

$$u = \partial_y \psi, \qquad v = -\partial_x \psi$$ (14)

in both phases. The solutions are exponentials in the time and streamwise coordinates, i.e.

$$\psi_1(x, y, t) = \exp(i(\alpha x - \omega t))\phi(y) \quad (y < 0),$$ (15)
$$\psi_2(x, y, t) = \exp(i(\alpha x - \omega t))\chi(y) \quad (y > 0).$$ (16)

With this Ansatz, we obtain two Orr-Sommerfeld equations for the functions $\phi(y)$ and $\chi(y)$, which are coupled at the interface. For the spatial problem, one solves the eigenvalues as complex wavenumbers α in terms of real frequencies ω. For the temporal problem, one solves the eigenvalues as complex frequencies ω in terms of real wavenumbers α.

For the numerical treatment it is advantageous [14] to consider the formulation in which only derivatives up to the second order are used : in fluid 1 (the lower liquid layer) we then have

$$\xi(y) = \left(\frac{\partial^2}{\partial y^2} - \alpha^2\right)\phi(y),$$

$$\left[(-i\omega + i\alpha U_1) - \frac{r}{m}\frac{1}{R}\left(\frac{\partial^2}{\partial y^2} - \alpha^2\right)\right]\xi(y) - i\alpha U_1''\phi(y) = 0,$$

and the equations for fluid 2 (the upper gas layer) are

$$\zeta(y) = \left(\frac{\partial^2}{\partial y^2} - \alpha^2\right)\chi(y),$$

$$\left[(-i\omega + i\alpha U_2) - \frac{1}{R}\left(\frac{\partial^2}{\partial y^2} - \alpha^2\right)\right]\zeta(y) - i\alpha U_2''\chi(y) = 0.$$

Here the variable R stands for the Reynolds number defined as

$$R = \frac{\rho_2 U_2^* \delta_2}{\mu_2}$$ (17)

In addition, the boundary conditions should be introduced. First at walls

$$\phi(-L_1) = \frac{\partial\phi}{\partial y}(-L_1) = 0 \quad \text{and} \quad \chi(L_2) = \frac{\partial\chi}{\partial y}(L_2) = 0.$$

and also at the interface $y = 0$. At this location, conditions have to be imposed. The continuity of spanwise and streamwise velocity components reads

$$\phi = \chi$$

and

$$\phi' + \frac{\alpha\phi}{\omega - \alpha U_0}U_1' = \chi' + \frac{\alpha\chi}{\omega - \alpha U_0}U_2',$$

where $'$ denotes differentiation with respect to y and

$$U_1(0) = U_2(0) \equiv U_0.$$

The continuity of tangential and normal stresses respectively take the form

$$\xi + 2\alpha^2\phi = m\left[\zeta + 2\alpha^2\chi\right]$$

$$\xi' - 2\alpha^2\phi' + iR(\omega - \alpha U_0)\phi' + i\alpha RU_1'\phi$$
$$-m\left[\zeta' - 2\alpha^2\chi'\right] - iRr(\omega - \alpha U_0)\chi'$$
$$-i\alpha RrU_2'\chi + i\alpha^2 R\left(F + \alpha^2 S\right)\frac{\phi}{\omega - \alpha U_0} = 0.$$

where the dimensionless numbers

$$S = \frac{1}{We} = \frac{T}{\rho_2(U_2^*)^2\delta_2} \quad \text{and} \quad F = \frac{g\delta_2}{(U_2^*)^2}(r - 1)$$

quantify the effects of surface tension T and gravity, respectively. In the following, gravity and surface tension are assumed to be negligible, i.e., $S = F = 0$.

The Orr-Sommerfeld eigenvalue problem is solved numerically using a Chebyshev collocation method [15]. In the numerical computation, we set $L_1 = L_2 = \infty$, and the Chebyshev collocation points map the interval $(-\infty, \infty)$ using the relation

$$[-1, 1] \mapsto (\mp\infty, 0]: \qquad y = \pm c\ln\left(\frac{1 + \eta}{2}\right),$$

where the upper sign holds for the liquid layer 1 and the lower sign for the gas layer 2 respectively. Here $c = 10$ is used. The resulting general linear algebraic eigenvalue problem is coded in Fortran and solved in double precision with the LAPACK routine ZGGEV. For the temporal calculations we typically use $N = 150$ Chebyshev polynomials per layer. In the spatial case the resolution is reduced to about $N = 100$ since the matrix used for the eigenvalue solver is of a larger size for the spatial problem than for the temporal problem with an identical number of Chebyshev polynomials.

ONE-LAYER LIMIT CASE

To validate the Chebyshev collocation spectral code, we recompute the spatial inviscid stability results by Huerre and Monkewitz [16] for a one-layer hyperbolic tangent profile

$$U(y) = 1 + M\tanh(y), \quad (-\infty < y < \infty)$$

where

$$M = \frac{U_2^\infty - U_1^\infty}{U_2^\infty + U_1^\infty}$$

is the velocity ratio and U_1^∞ and U_2^∞ are the velocities of the two co-flowing streams. If $M < 1$ both fluids move in the same direction ($U_1^\infty, U_2^\infty > 0$) and if $M > 1$ there is reverse flow, e.g. $U_1^\infty < 0$, and $U_1^\infty = 0$ if $M = 1$. Huerre and Monkewitz found that the velocity ratio M governs either the transition from the convective or absolute instability: there exists a critical value $M_c \approx 1.315$ such that if $M < M_c$ the flow is convectively unstable and if $M > M_c$ the flow is absolutely unstable [16]. We obtain precisely the same result using our
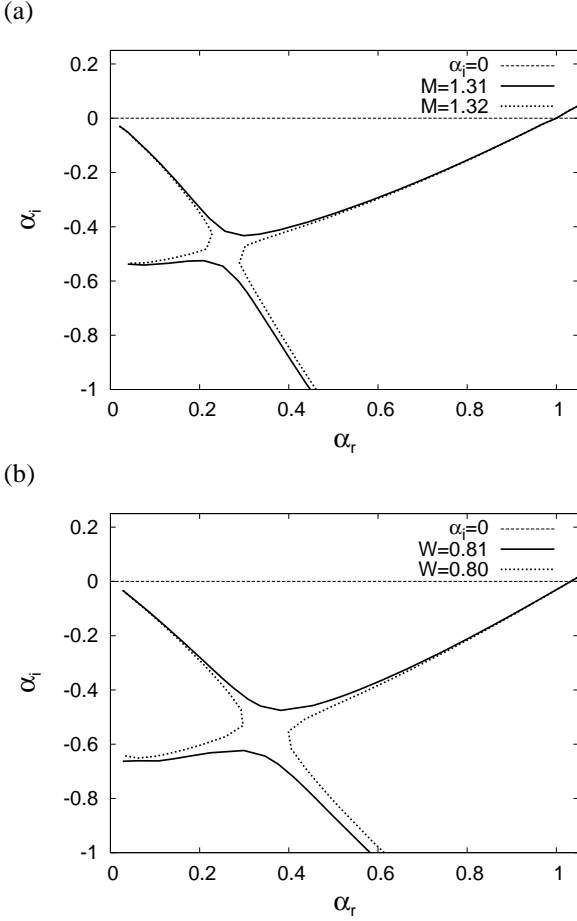
(a)

(b)

Figure 3: Spatial instability results in the one-layer limit for (a) tanh profile and (b) the error-function profile both for $r = m = n = 1$. $R = 1000$.

code in the one-layer limit $r = m = n = 1$ and $S = F = 0$ for large Reynolds numbers and replacing the error-function or generalized profiles by the tanh profile (Figure 3(a)).

In the one-layer limit, the spatial instability for the profile (1,2) is shown in Figure 3(b). The velocity ratio M can be related to V and W through the relationship

$$M = \frac{U_2^\infty - U_1^\infty}{U_2^\infty + U_1^\infty} = \frac{(W+V) - (W-1)}{(W+V) + (W-1)} = \frac{V+1}{2W+V-1}.$$

It can be seen, that if $W > 1$ (or equivalently $M < 1$) both fluids move in the same direction and if $W < 1$ (or $M > 1$) there is reverse flow, e.g. the liquid moves to the left. In the limiting case $W = 1$ (or $M = 1$) the liquid phase is at rest at infinity.

Let us denote by W_c the critical value such that if $W > W_c$ the flow is convectively unstable and if $W < W_c$ the flow is absolutely unstable. To obtain this value one starts computing the spatial branches $\alpha^{(j)}$ at a large value of W (such that the flow is surely convectively unstable). This is performed by varying the real frequency ω. One then follows such branches by further reducing the value of W until a cusp appears connecting two different types of spatial branches (some care should be exerted here to avoid some non-pertinent branch crossing). The critical value is found to be $W_c \approx 0.805$ for the error-function profile, or equivalently $M_c \approx 1.24$ (Figure 3(b)).

VISCOSITY STRATIFIED CASE WITH EQUAL DENSITIES

Viscosity stratification gives rise to an additional instability mechanism which may significantly change the results in comparison with the one-phase shear layer. Indeed an additional unstable mode called H-mode is introduced in the temporal stability case [9]. We hence examine, for the error-function velocity profile with matched densities $r = 1$ and equal boundary layer sizes ($n = 1$), how the stability characteristics are modified when the viscosity ratio m is decreased from $m = 1$. Surface tension is neglected ($S = 0$).
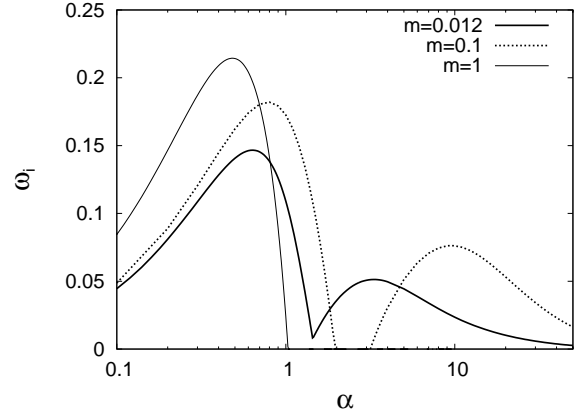

Figure 4: Temporal stability results depending on the vicosity ratio m: error-function profile for r=n=1, R=1000 and various values of m.

The temporal growth rate ω_i is shown as function of the real wavenumber α in Figure 4 for fixed $R = 1000$ and different m. By comparing the cases $m = 1$ and $m = 0.1$ a separate unstable mode with a maximum of ω_i around $\alpha = 10$ can be clearly identified at $m = 0.1$. It is also present at $m = 0.012$ with the maximum appearing at smaller α. We have verified by variation of R that this additional mode shows the typical scaling with the Reynolds number of the H-mode. The wavenumber $\alpha_{\max}$ of maximum amplification ω_i increases as

$$\alpha_{\max} \sim \sqrt{R} \qquad (18)$$

because the characteristic length scale of the instability is set by the viscous diffusion length based on the shear rate $S_2 \sim U_2^*/\delta_2$ at the interface. This lengthscale is

$$\sqrt{\frac{\mu_2/\rho_2}{S_2}} \sim \frac{\delta_2}{\sqrt{R}}. \qquad (19)$$

Starting from these temporal instability results we have performed spatial stability calculations at fixed $R = 1000$ in order to detect the threshold for absolute instability. To identify absolute instability we have again computed the spatial branches $\alpha^{(j)}(\omega)$ for real frequency ω starting at sufficiently large W to ensure that the flow is convectively unstable. The results are shown in Figures 5(a-c). Comparing Figure 5(b) and Figure 5(c) with the one-phase result of Figure 5(a) we find spatial branches corresponding to the H-mode of the temporal calculations. For $m = 0.1$ and $m = 0.012$ we observe the formation of a cusp between two spatial branches originating in the upper and lower half-plane for the H-mode. Remarkably, the absolute instability appears without reversed flow in fluid 1 ($W_c > 1$) for $m = 0.012$.
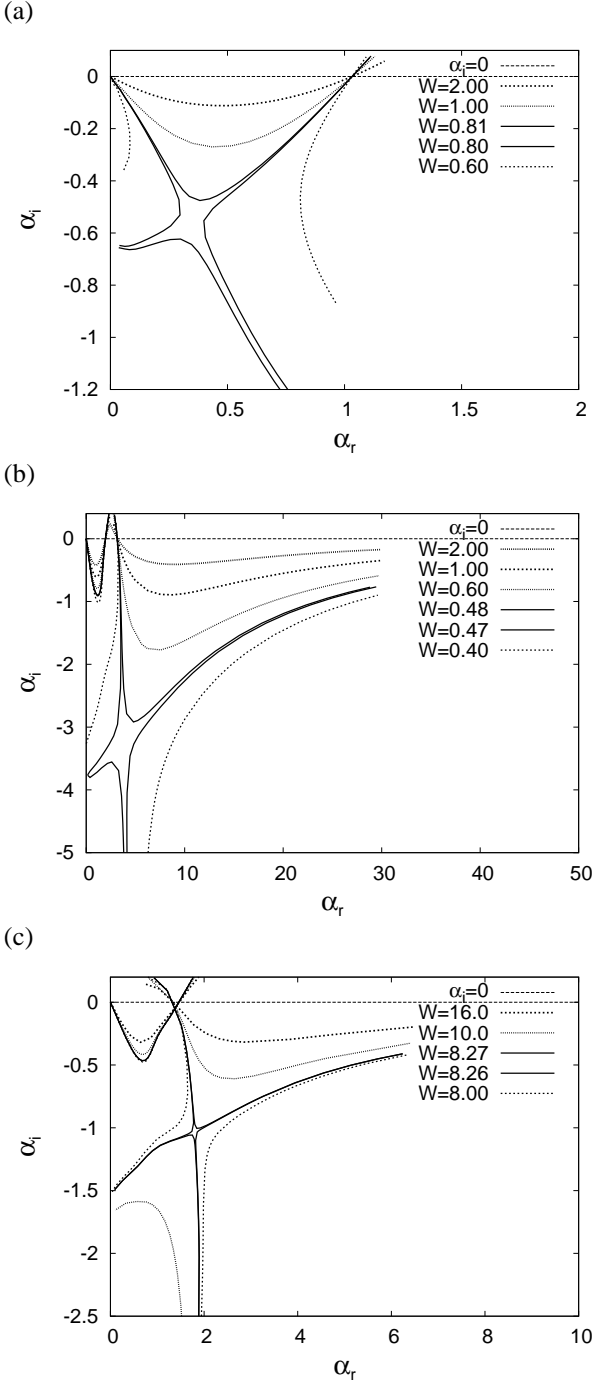
4

(a)

(b)

(c)

Figure 5: Spatial instability results in the viscosity stratified case for the error-function profile, r=n=1, R=1000 and (a) m=1, (b) m=0.1, (c) m=0.012.

RESULTS FOR UNEQUAL DENSITIES AND VISCOSITIES

In this section, we evaluate the importance of the velocity defect for the instability by comparing the results obtained in the case of the error function profile and the generalized profile. We choose density and viscosity ratios corresponding approximately to air and water, namely $r = 0.0012$ and $m = 0.012$ and we keep the boundary layer sizes equal ($n = 1$) and neglect the influence of surface tension ($S = 0$). The parameter V is here free for the generalized profile, bur we shall consider here only the value $V = n/m$.

Temporal linear stability analysis results are shown in Figures 6(a,b) at $R = 1000$ for the error-function profile and the
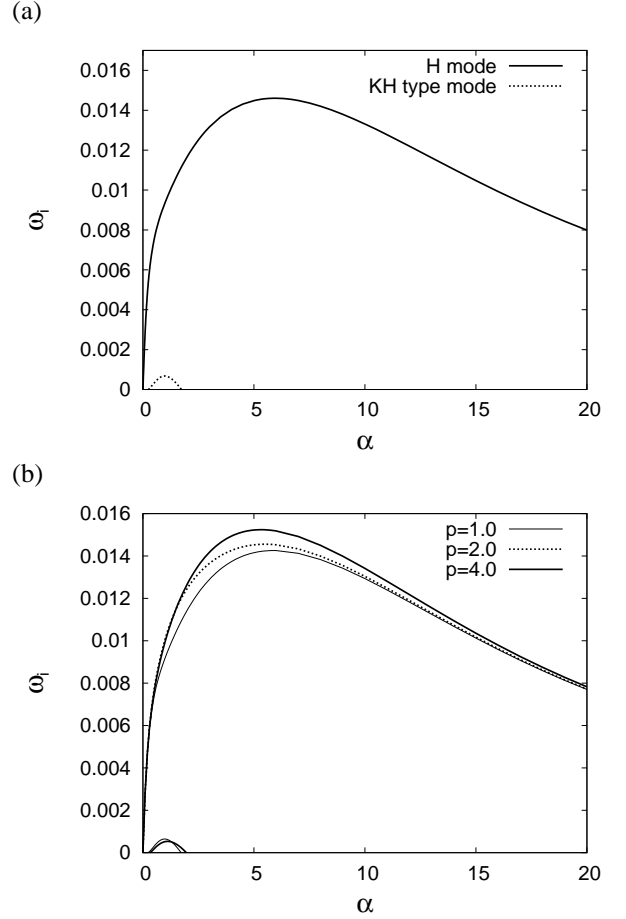
(a)

(b)

Figure 6: Temporal stability results (a) for the error-function profile, (b) for the generalized profile both for $r = 0.0012, m = 0.012, n = 1, R = 1000$.

R	ω_i^{max}	α^{max}
1000	0.014604	6.0
2000	0.014608	8.4
10000	0.014616	18.9
40000	0.014774	38.5
160000	0.014299	73.9

Table 1: Maximum temporal amplification rate ω_i^{max} and corresponding wavenumber α^{max} of the H-mode for the error-function velocity profile: $r = 0.0012, m = 0.012, n = 1$.

generalized profile. In Figure 6(a) two unstable modes are present. The least stable mode again shows the square root dependence on the Reynolds number for the wavenumber of maximum growth, which is shown in Table 1. It corresponds to the H-mode. We notice that another unstable mode is present as well, which should be related to the inviscid Kelvin-Helmholtz mechanism. However, it can probably not be considered as a "pure" inviscid Kelvin-Helmholtz mode due to mode "mixing" at finite values of R [9]. For larger Reynolds numbers, the situation is more complicated since up to four unstable modes can appear and mode exchange is possible as observed in Ref. [9].

The change from the error-function profile to the generalized profile with velocity defect causes no significant change in the temporal stability characteristics as seen from the comparison between Figure 6(a) and Figure 6(b). The H-mode is again the most unstable one, and its peak is only slightly shifted upon increasing the parameter p (which enhances the velocity defect).
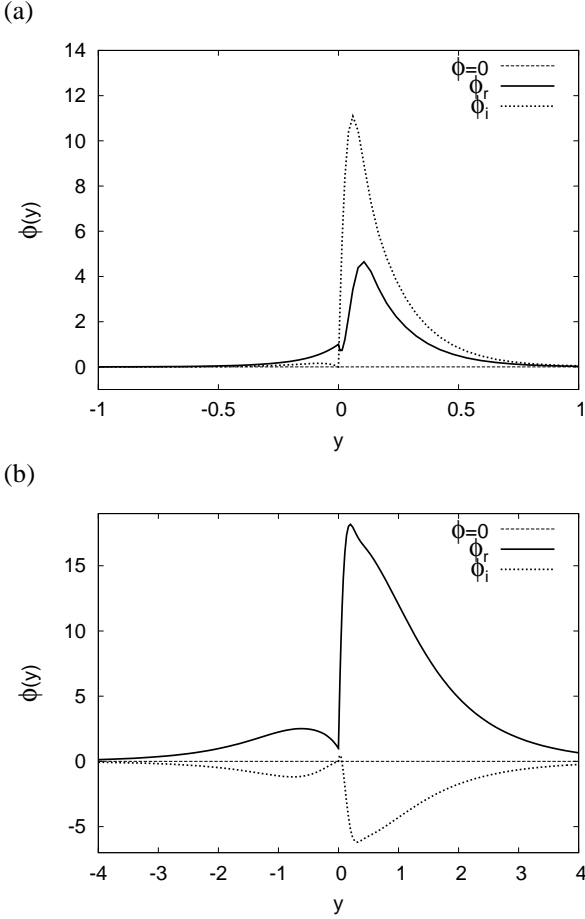
(a)

(b)

Figure 7: Temporal eigenfunctions for the error-function profile at wavenumbers with maximum amplification rate: (a) H mode at $\alpha = 6.0$, (b) Kelvin-Helmholtz type mode at $\alpha = 1.0$ both for $r = 0.0012, m = 0.012, n = 1, R = 1000$.
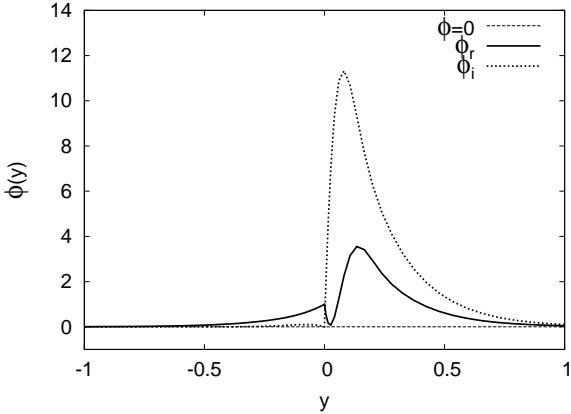

Figure 8: Temporal eigenfunctions of the H mode for the generalized profile ($p = 4$) at the wavenumber with maximum amplification rate $\alpha = 5.3$ for $r = 0.0012, m = 0.012, n = 1, R = 1000$.

The weaker unstable mode is also present at $p = 1$. It becomes stable at $p = 2$ but reappears as unstable mode for $p = 4$.

The structure of eigenfunctions is shown in Figures 7(a,b) for the error-function profile. For the H-mode shown in Figure 7(a) the velocity perturbation is strongest in the gas, which can be expected because of the large viscosity contrast. For the second unstable mode shown in Figure 7(b) the discrepancy between gas and liquid is less pronounced because of the different phys-

ical mechanism. For the eigenfunctions corresponding to the H-mode, the the generalized profile and the error function profile produce fairly similar results, as can be seen by comparing Figure 7(a) and Figure 8.
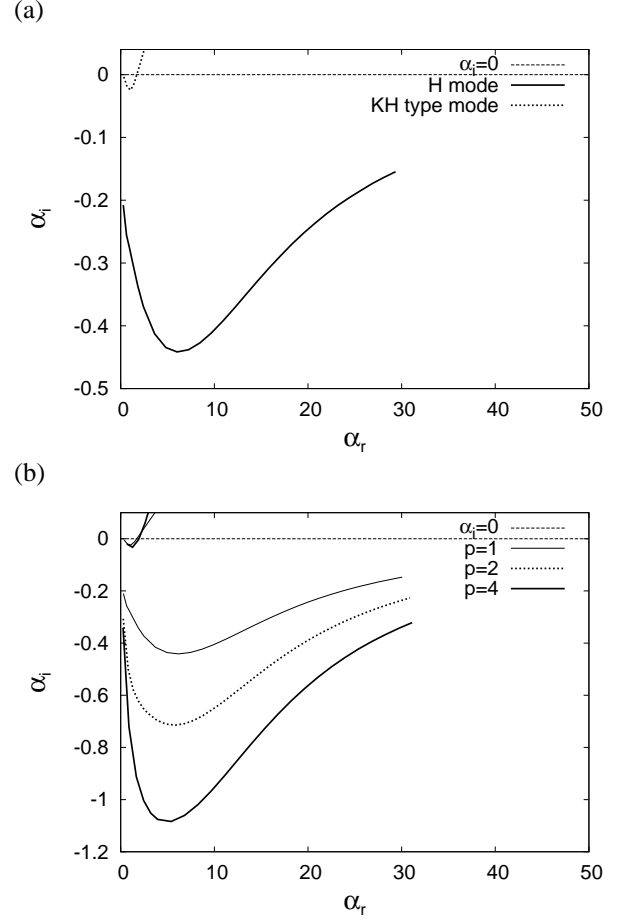
(a)

(b)

Figure 9: Spatial instability results (a) for the error-function profile (W=2.72), and (b) for the generalized profile (W=0.68) both for $r = 0.0012, m = 0.012, n = 1, R = 1000$. W is chosen such that $U_2^\infty/U_1^\infty = 50$.

In summary, the introduction of the velocity defect does not modify the temporal stability results significantly in the present case. We shall now consider the spatial problem with a prescribed velocity ratio $U_2^\infty/U_1^\infty = 50$, which corresponds to typical values in atomization experiments for the planar geometry performed by the group at LEGI (Laboratoire des Ecoulements Geophysiques et Industriels) at the Institut National Polytechnique de Grenoble (INPG) [4]. This way, the offset velocity W is fixed for both types of velocity profiles for given m, n and V.

The spatial stability computations demonstrate that the instability remains convective for these parameters. Figure 9(a) shows the two unstable spatial branches $\alpha^{(j)}(\omega)$ for the error function profile, which correspond to the unstable temporal modes of Figure 6(a). They are again identified as H-mode and Kelvin-Helmholtz type mode in the legend. Unstable spatial branches for the generalized basic velocity profile are shown in Figure 9(b) for different values of the parameter p, which characterizes the size of the velocity defect on the interface. It turns out that the maximal spatial growth rate $\alpha_i^{\max}$ associated with the H-mode increases significantly with the size of the velocity defect. As in the temporal stability computations, the second unstable branch is present at $p = 1$ and $p = 4$ but disappears for $p = 2$. In spite of the enhanced spatial growth rate, the structure
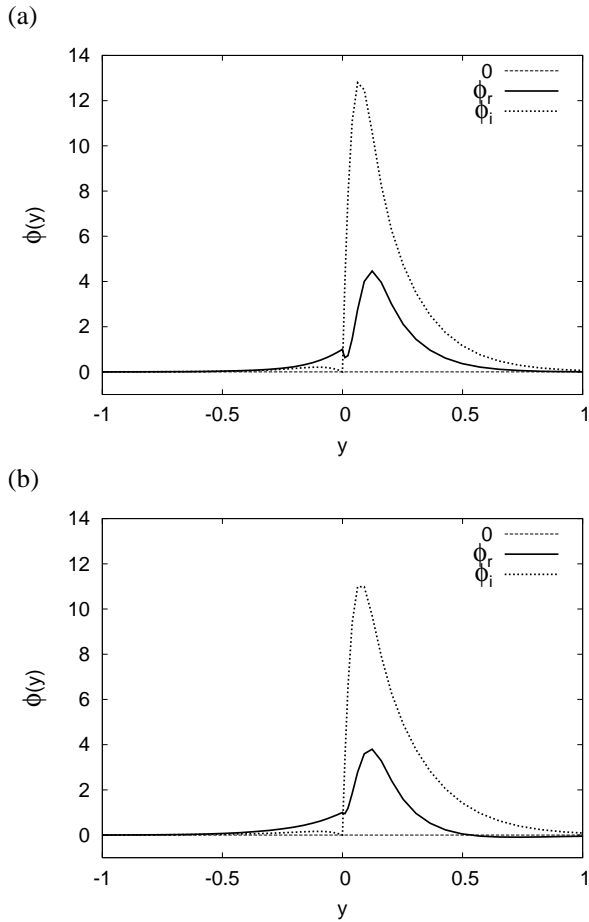
Figure 10: Spatial eigenfunctions of the H mode at frequency with maximum spatial amplification rate (a) for the erf profile at $\omega = 0.20$, (b) for the generalized basic velocity profile (p=4) at $\omega = 0.08$ both for r=0.0012, m=0.012, n=1, R=1000.

of the eigenfunctions is not changed significantly by the introduction of the velocity defect. This can be seen in Figure 10, which shows the spatial eigenfunctions for the error function profile and the generalized velocity profile.

CONCLUSIONS

We have studied the spatial and temporal linear stability of viscous two-phase mixing layers with finite boundary layer sizes and velocity defect. Surface tension effects were neglected in order to highlight the role of the instability mechanism by Hooper and Hinch [10, 11], which produces an additional unstable mode at short wavelength called the H-mode. The spatial/temporal Orr-Sommerfeld eigenvalue problems have been discretized with a Chebyshev collocation method in each fluid. For matched densities and without the velocity defect the H-mode can cause absolute instability without reverse flow when the viscosity contrast is sufficiently large. With density and viscosity ratios approximately corresponding to air and water the H-mode remains dominant in the absence of surface tension. The presence of a velocity defect does not modify the temporal stability results in this case, but the spatial growth rates increase substantially. The spatial growth rates also turn out to be significantly larger than predicted on the basis of the Gaster transformation [17]. In the case corresponding to Figure 9(a) the prediction of the maximum growth rate is approximately 10^{-2} of the real spatial growth rate obtained by solving the spatial

eigenvalue problem. This failure has been previously pointed out for velocity profiles with inflection points in the one-phase case [18].

In continuation of the present work we plan a systematic study of the various parameter influences on the spatial instability. In particular, surface tension has be taken into account in order to allow a comparison with experimental results.

REFERENCES

[1] J. C. Lasheras and E. J. Hopfinger. Liquid jet instability and atomization in a coaxial gas stream. *Annu. Rev. Fluid Mech.*, 32:275–308, 2000.

[2] P. Marmottant and E. Villermaux. On spray formation. *J. Fluid Mech.*, 498:73–111, 2004.

[3] M. Ghorokhovski and M. Herrmann. Modelling primary atomization. *Annu. Rev. Fluid Mech.*, 40:343–366, 2008.

[4] F. Ben Rayana. *Étude des instabilités interfaciales liquide-gaz en atomisation assistée et tailles de gouttes*. PhD thesis, Institut National Polytechnique de Grenoble, 2007.

[5] T. Boeck, J. Li, E. Lopez-Pages, P. Yecko, and S.Zaleski. Ligament formation in sheared liquid-gas layers. *Theoretical and Computational Fluid Dynamics*, 21:59–76, 2007.

[6] R. R. Nourgaliev, M. S. Liou, and T. G. Theofanous. Numerical prediction of interfacial instabilities: Sharp interface method. *J. Comp. Phys.*, 227:3940–3970, 2008.

[7] E. Villermaux. Mixing and spray formation in coaxial jets. *Journal of Propulsion and Power*, 14:807–817, 1998.

[8] P. Yecko, S. Zaleski, and J.-M. Fullana. Viscous modes in two-phase mixing layers. *Phys.Fluids*, 14:4115–4122, 2002.

[9] T. Boeck and S. Zaleski. Viscous versus inviscid instability of two-phase mixing layers with continuous velocity profile. *Phys. Fluids*, 17:032106, 2005.

[10] A. P. Hooper and W. G. C. Boyd. Shear-flow instability at the interface between two viscous fluids. *J. Fluid Mech.*, 128:507–528, 1983.

[11] E.J. Hinch. A note on the mechanism of the instability at the interface between two shearing fluids. *J. Fluid Mech.*, 144:463–465, 1984.

[12] M. P. Juniper and S. Clandel. The stability of ducted compound flows and consequences for the geometry of coaxial injectors. *J. Fluid Mech.*, 482:257–269, 2003.

[13] M. P. Juniper. The effect of confinement on the stability of two-dimensional shear flows. *J. Fluid Mech.*, 565:171–195, 2006.

[14] J. J. Dongarra, B. Straughan, and D. W. Walker. Chebyshev tau-QZ algorithm methods for calculating spectra of hydrodynamic stability problems. *Applied Numerical Mathematics*, 22:399–434, 1996.

[15] P. J. Schmid and D. S. Henningson. *Stability and Transition in Shear Flows*. Springer, New York, 2001.

[16] P. Huerre and P.A. Monkewitz. Absolute and convective instabilities in free shear layers. *J. Fluid Mech.*, 159:151–168, 1985.

[17] M. Gaster. A note on the relation between temporally-increasing and spatially-increasing disturbances in hydrodynamic stability. *J. Fluid Mech.*, 14:222–224, 1962.

[18] W. O. Criminale, T. L. Jackson, and R. D. Joslin. *Theory and Computation of Hydrodynamic Stability*. Cambridge University Press, Cambridge, 2003.